UNIVERSITYOF BIRMINGHAM

Research at Birmingham

CSP plants with thermocline thermal energy storage and integrated steam generator – Techno-economic modeling and design optimization

Pizzolato, A.; Donato, F.; Verda, V.; Santarelli, M.; Sciacovelli, Adriano

Link to publication on Research at Birmingham portal

Accepted Manuscript

CSP plants with thermocline thermal energy storage and integrated steam generator – Techno-economic modeling and design optimization

A. Pizzolato, F. Donato, V. Verda, M. Santarelli, A. Sciacovelli

Please cite this article as: A. Pizzolato, F. Donato, V. Verda, M. Santarelli, A. Sciacovelli, CSP plants with thermocline thermal energy storage and integrated steam generator – Techno-economic modeling and design optimization, *Energy* (2017), doi: 10.1016/j.energy.2017.07.160
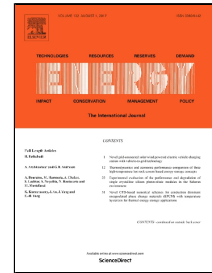
CSP plants with thermocline thermal energy storage and integrated steam generator – Techno-economic modeling and design optimization

A. Pizzolato[a], F. Donato[b], V. Verda[a], M. Santarelli[a], A: Sciacovelli[c]

[a] Department of Energy, Politecnico di Torino, Corso Duca degli Abbruzzi 24, 10129, Torino, Italy, alberto.pizzolato@polito.it, 0110904478

[b] ENEA UTRINN Via Anguillarese 301, 00123 Rome, Italy

[c] School of Chemical Engineering., Birmingham Centre for Energy Storage (BCES), University Of Birmingham, UK

Abstract

Although CSP has reached technological maturity, high capital investment and specific electricity cost remain the major development barriers. To reduce them, highly efficient, integrated, and cheaper CSP components are urgently needed. In this paper, we investigate a novel CSP plant configuration with a single-tank Thermal Energy Storage (TES) fully integrated with the steam generator.

The objective of this research is twofold: i) provide a reliable model of single-tank thermal storages with integrated steam generator; ii) identify two optimized CSP plant designs to achieve best energetic and economic performances. To achieve these aims we developed a numerical model of the main system components and validated it against experimental data. This model was then integrated in a full simulation and heuristic design optimization of the plant.

The results revealed that the system proposed can generate electricity in middle-Italy (Rome) at a cost of 230.25 \$/MWh with a 15 % reduction compared to the double tank option. Furthermore, if cogeneration is used to recover the waste heat, this system is an interesting option for users such as small districts, university campuses and hospitals. In the latter case, the optimized system pays off in 6 years and covers 80 % of the heating and cooling requirements.

Highlights

- A novel CSP plant with thermocline TES and integrated steam generator is modeled in details
- The solar field and the integrated TES models are validated with experimental data
- The single tank configuration lowers the LEC of 42 \$/MWh
- Cogeneration lowers the LEC of 28 %

31   **Keywords:** Concentrated Solar Power; Integrated Steam Generator; Molten Salts; Techno-economic
32   Optimization; Thermocline Energy Storage;

33   **Nomenclature**

34   **Latin letters**

A	Area $[m^2]$	
C	Cost [\$]	
c_p	Specific Heat $\left[\frac{\text{J}}{\text{kgK}}\right]$	
C_y	Yearly cost $\left[\frac{\$}{\text{year}}\right]$	
d	Diameter [m]	
E	Yearly Electrical energy$\left[\frac{\text{MWh}}{\text{year}}\right]$	
$\dot{E}$	Electrical power [W]	
e	Specific kinetic energy $\left[\frac{\text{J}}{\text{kg}}\right]$	
Eu	Euler number [-]	
FIT	Feed-In Tariff $\left[\frac{\$}{\text{MWh}}\right]$	
f_{labor}	Labor cost index ratio$[\,-\,]$	
$f_{M\&S}$	Marshall & Swift cost index ratio $[\,-\,]$	
h	Specific enthalpy $\left[\frac{\text{J}}{\text{kg}}\right]$	
k	Thermal conductivity $\left[\frac{\text{W}}{\text{m K}}\right]$	
k_l	Geometric factor for helicoidal heat exchangers [-]	
L	Length $[m]$	
LEC	Levelized Electricity Cost $\left[\frac{\$}{\text{MWh}}\right]$	
m	Mass flow rate $\left[\frac{kg}{s}\right]$	
n	Scale factor $[\,-\,]$	
Nu	Nusselt number [-]	
p	Pressure [Pa]	
Pr	Prandtl number [-]	
Q	Yearly Thermal Energy $\left[\frac{\text{GJ}}{\text{year}}\right]$	
$\dot{Q}$	Thermal power [W]	

R	Revenues [\$]	
Re	Reynolds number [-]	
R_y	Yearly revenues $\left[\frac{\$}{\text{year}}\right]$	
S	Characteristic size [-]	
$SPBT$	Simple Payback time [years]	
T	Temperature [K]	
t	Time [s]	
$TCLF$	Thermal Load Capacity Factor [–]	
U	Global heat transfer coefficient $\left[\frac{\text{W}}{\text{m}^2\text{K}}\right]$	
th	Thickness [m]	

35   **Greek letters**

α	Heat transfer coefficient $\left[\frac{\text{W}}{\text{m}^2\text{K}}\right]$
η	Efficiency [–]
ρ	Density $\left[\frac{\text{kg}}{\text{m}^3}\right]$

36   **Subscripts**

abs	Absorbed
b	Buoyancy
bc	Boundary condition
bl	Boling
cont	Contingencies
dec	Decommissioning
dir	Direct
ec	Economizer
el	Electrical
ev	Evaporator
f	Friction
Fo	Fouling
FW	Feed-water
h	Hydraulic
HTF	Heat Transfer Fluid
i	Internal

in	Incoming
inv	Investment
lam	Laminar
ls	Liquid-Solid phase transition
MS	Molten Salts
nom	Nominal
o	External
O&M	Operation and Maintenance
out	Outgoing
ref	Reference
SF	Solar Field
sh	Superheater
sol	Solar
t	Tube
th	Thermal
turb	Turbulent
y	Yearly

37

1   Introduction

39 Despite having been under investigation for several decades, Concentrated Solar Power (CSP) is still

40 hardly competitive with conventional fossil-based power plants and the expected market development

41 in the Mediterranean region remains an unfulfilled promise. The high upfront investment cost and the

42 difficult siting [1] are the two major barriers to a rising share of CSP in the future energy mix. It is

43 thus clear that the primary focus of future research should be the reduction of both the investment

44 cost and the specific cost of electricity, which will extend the CSP market also to mid-size plants

45 located at intermediate latitudes.

46 The first step in this direction is the simplification of the power plant loop. In this regard, ENEA

47 (Italian National Agency for New Technologies, Energy and Sustainable Economic Development)

48 has promoted [2] the use of a thermocline (i.e. single-tank) Thermal Energy Storage (TES) with an

49 integrated Steam Generator (SG) submerged in the heat storage medium. The plant can be further

50 simplified through the use of the molten salts mixture, which was commonly found as heat storage

51 medium, also as the Heat Transfer Fluid [3] with consistent benefits to the efficiency of the power

52 cycle.

The submerged steam generator technology is well-known within the nuclear community and many models have been developed in the past. For instance Ref. [4] proposed a lumped parameter approach considering three regions (i.e. the subcooled, the boiling and the superheater region) with movable boundaries, while in Ref [5] the Authors refined the discretization to get a 1D finite volume approach [6]. However, only a few studies [7], considered the natural circulation on the coolant side, with a design close to the submerged steam generator proposed by ENEA. Furthermore, literature is rich in thermocline TES model. For instance, Yang and Garimella [8] investigated the performance of a molten salts thermocline tank filled with quartzite rock through a 2D axial-symmetric finite volume model; they show that the discharge efficiency raises for tanks with a high aspect ratio and operated at small Reynolds number. Strasser et al. [9] adopted a similar approach to show that the cycle efficiency can be further enhanced with a structured concrete network instead of conventional packed bed material. The use of latent heat storage in CSP has also been studied in great details: Nithyanandam et al. [10] studied the performance of a packed bed TES with encapsulated PCM during partial charging and discharging cycles while Fornarelli et al. [11] developed a detailed numerical model of a shell-and-tube TES with Phase Change Material showing that natural convection can be conveniently exploited to reduce the melting time. Despite this great availability of literature on the topic, only Ref. [12] studied the integrated storage-steam generator system. The great level of detail of their finite volume model makes it ideal for technology development but impractical for system analysis and plant optimization, which demand for more compact modeling approaches.

For what it concerns the reduction of the specific cost of electricity, a possible field of competitiveness improvement for small CSP is represented by polygeneration. The option of CSP-driven desalination has been widely investigated [13 14], since regions with high water scarcity generally have a large solar resource. Another interesting cogeneration option is the CSP-driven biomass gasification, which has lately received considerable attention in the scientific community [15]. On the other hand, it should be noted that only a few researchers [16, 17] have investigated the cogeneration of power, heating and cooling in a single CSP plant, which could be an ideal opportunity to enlarge the market of CSP to users like small districts, university campuses and hospitals.

We believe that the innovative match of these two concepts, i.e. the ENEA compact system and the cogeneration option, has the potential to open the doors of CSP to small-scale facilities in regions with moderate solar resources. In order to quantify this potential, in this paper we utilize the tools of energy and economic analysis, which have been proficiently applied in the past to solar tower combined cycle [18, 19], parabolic through plants for process heat generation [20] and to CSP desalination plants [21].

87 This paper stems from the need of filling the literature gaps we highlighted in this introduction.

88 Firstly, we aim at providing a reliable (i.e. validated with experimental data) and computationally

89 cheap (i.e. suited for system-level annual simulations) modeling framework of the storage tank with

90 integrated steam generator. Secondly, this paper has the objective of proposing two optimized designs

91 of the small CSP cogeneration system as well as to analyze their performances. The first design is

92 thought for an ideal thermal user and has the aim of establishing the potential of the technology. The

93 second one is targeted to a specific user, i.e. a hospital, and has the aim to analyze the performances

94 of the system when coupled with a real user in a real energy market.

95 ## 2 The CSP cogeneration plant with thermocline TES and integrated Steam Generator

96 ### 2.1 Power plant description

97 Figure 1 presents the system proposed by ENEA. The molten salts pump (MSP) circulates the "solar

98 salt" (i.e. an eutectic mixture with 60 wt % $NaNO_3$ and 40 wt % KNO_3) from the storage tank into

99 the receiver tubes of the Parabolic Trough Solar Collectors (PTSC) (streams 1, 2 and 3). Once the

100 fluid reaches the desired temperature (stream 4), it is circulated back to the storage tank (stream 6).

101 If the system conditions do not allow to reach the desired temperature the salts can be circulated back

102 to the solar collectors with a by-pass valve (stream 5). The storage tank contains a steam generator,

103 which is immersed in the molten salts; this sub-system is called Storage Tank with Integrated Steam

104 Generator (STISG). The steam produced (stream 7) flows to the steam turbine and it is eventually

105 condensed in the condenser (WCD) (stream 8). In cogeneration mode, the thermal power collected

106 by the steam condenser (stream 11) is used to satisfy the thermal requirements of a heat consumer or

107 can be fed to an Absorption Chiller Unit (ACU) to satisfy a cooling load. Finally, the Rankine cycle

108 is closed with the use of a water pump (WP1).

109 In the following sections, a summary of the modelling approach of the three main subsystems of the

110 plant is given, namely the solar field, the STISG and the power block. The modeling approach utilized

111 in this paper results from a trade-off between fidelity of the system representation, complexity of

112 input data needed to model a real installation and computational effort required for the design

113 optimization of such a complex system. The good agreement with experimental results suggests the

114 validity of the modeling assumptions and the correctness of the code implementation.

115 ### 2.2 Main assumptions

116 The following assumptions have been made to model the plant:

117 • The maximum design temperature in the receiver is set to 550 °C. This value is suggested

118 based on the experience maturated at the 5 MW Archimede plant in Priolo Gargallo [22]. At

119 higher temperatures, alkaline hydroxides and carbonates are produced at higher rate. These
120 species present a limited solubility in molten nitrates and precipitate rapidly yielding to pipes
121 and valves occlusion.

122 • The high pressure level of the steam cycle has been fixed to 40 bar.

123 • The condenser minimum driving temperature difference, i.e. at the pinch point, has been set
124 to 10 °C.

125 • The temperature required by the waste heat recovery unit (stream 12) has been set equal to 90
126 °C.

127 • The efficiency of the heat distribution system is set to 90 % and the Coefficient of Performance
128 of the absorption chiller to 60 %, as suggested as a reasonable value for single effect Water-
129 LiBr absorption machines (e.g. in [23]). This means that, in winter, 90 % of the recovered
130 heat is available as heating power, while, in summer, 60 % of the recovered is available as
131 cooling power. Distribution losses are neglected.

132 **3 Mathematical modelling of the power plant components**

133 **3.1 Solar field**

134 *3.1.1 Components description and Model*

135 We have modeled a concentrator similar to the one already in operation at the Archimede plant [22].
136 The parabolic through reflector is a 12.5 m long parabolic mirror with 5.76 m of aperture and a focal
137 height of 2.01 m. It sustains a 4.06 m long receiver tube consisting of an absorber inside a glass
138 envelope with bellows at either end. The absorber is a stainless steel tube (70 mm in diameter) which
139 is treated with selective coating to obtain a high absorptance in the solar energy spectrum, and low
140 emittance in the infrared (i.e. 95% and 7.3% respectively from manufacturer specifications). The
141 glass envelope (125 mm in diameter) is made of Pyrex and guarantees a transmittance higher than 96
142 % in the full range of operating temperatures. The annulus space between the absorber and the glass
143 envelope is under vacuum (1 x 10^{-4} mbar) to reduce thermal losses.

144 In the present work, the analytical equations of Ref. [24] are used for the solar position and the optical
145 model of the receiver while a more detailed approach is followed for the thermal model of the receiver
146 tube. A quasi 1D model is implemented: the receiver is discretized along the axial direction and, for
147 each of the finite volume, a thermal balance is written considering non-advective heat transfer (i.e.
148 conduction and radiation) only in the radial direction. This approach is widely used for the simulation
149 of thermal systems of this type [24, 25]

150 Specifically, the formulation presented in Ref. [25] is considered: assuming steady-state and for a

151 negligible change in potential energy we can write:

152 $$\dot{Q}_{net} = \dot{m}_{HTF}\left(h_{in} + e_{in} - h_{out} - e_{out}\right) \tag{1}$$

153 $\dot{Q}_{net}$ is the radiative power effectively transferred to the heat transfer fluid and can be calculated as:

154 $$\dot{Q}_{net} = \dot{Q}_{abs} - \dot{Q}_{losses} \tag{2}$$

155 In steady-state conditions, the concentrated radiation absorbed on the surface of the absorber tube can

156 be either transmitted to the heat transfer fluid or rejected towards the environment. In the first case,

157 we have a series of the following thermal resistances (Fig. 2)

158 • Conduction from the outer surface of the absorber tube to the inner surface of the absorber
159 tube

160 • Convection from the inner surface of the absorber tube the heat transfer fluid

161 In the second case, the thermal power path is the following (Fig. 2):

162 • Radiation/convection heat transfer from the outer surface of the absorber tube to the inner
163 surface of the glass envelope

164 • Conduction heat transfer across the glass envelope

165 • Radiation/convection heat transfer from the external surface of the glass envelope towards the
166 environment

167 The thermal properties of the materials and the correlations proposed in [25] were used for the

168 calculation of the heat transfer coefficients. The irradiance data were obtained from the HelioClim3

169 database [26] and the wind speed and ambient temperature data from the EnergyPlus database [27],

170 both providing data with a 15 minutes sampling.

171 *3.1.2 Experimental validation*

172 The test bench consists of a 50 meters parabolic though solar field, similar to the one described in the

173 modeling section of this paper. The experimental string is composed by 4 reflectors in series. Four

174 thermocouples are soldered on the external surface of the receiver tube at each joint between consecutive

175 reflectors. Two submerged thermocouples are placed at the inlet and at the outlet of the experimental facility,

176 i.e. at x = 0 m and at x = 50 m respectively. The soldered thermocouples provide a highly varying measurement

177 along the angular coordinate which cannot be accounted for in our quasi 1D model. Hence, only the

178 measurements provided by the submerged thermocouples is used. The measurement at x = 0 m provides the

179 inlet boundary condition while the measurement at x = 50 m is used to validate the model. Figure 3 compares

180 temperature measured at x = 50 m with values predicted by our numerical model. The average mass

181 flow rate during the test is 6.39 kg/s with a standard deviation of 0.23 kg/s.

182 The largest difference between experimental and numerical results arises when the inlet temperature

183 is varied over the duration of the test because the model does not account for transient effect, while a

184 good approximation is visible during steady-state conditions. Nevertheless, a steady-state model

185 remains suitable to reproduce the normal operating conditions of a commercial CSP plant, where the

186 mass flow rate is varied by the control system to maintain a constant temperature levels across the

187 receiver tubes. The average first law efficiency is calculated as 0.54 with a standard deviation of 0.05.

188 **3.2   Storage tank with integrated steam generator**

189 *3.2.1   Component description and model*

190 The steam generator is a once-through counterflow shell-and-tube heat exchanger with a helicoidal

191 tube bundle: on the shell-side, in an annulus-shaped channel, the molten salts flow downward and,

192 on the tube side, water flows upward becoming superheated steam. This heat exchanger operates in

193 natural circulation mode on the molten salts side thanks to the strong fluid; in fact, within the range

194 of temperatures considered, the density of the fluid experiences nearly a 10 % variation which is

195 exploited as motion driving force.

196 Figure 4 schematically illustrates the STISG system for the small CSP cogeneration plant described

197 in Section 2.

198 The temperature of fluids along the axial dimension of the steam generator are calculated with a one-

199 dimensional finite volume numerical model [28] using a double iteration loop to solve the natural

200 circulation problem (Figure 5):

201   1. The molten salts mass flow is guessed

202   2. The outlet temperature of the molten salts (bottom side of the steam generator) is guessed

203   3. The thermal problem is solved following a fist-order upwind approximation on the water side

204   until the temperatures of the two fluids in the upper side of the steam generator are obtained,

205   i.e. the molten salts inlet temperature and the steam outlet temperature

206   4. The calculated inlet temperature of the molten salts is compared with the boundary condition.

207   If the convergence criterion is not met, a new outlet temperature is calculated and the code

208   returns to step 3. Otherwise, the algorithm is allowed to proceed to step 5.

209   5. The pressure drop on the molten salts side is calculated and it is compared to the buoyancy

210   pressure difference. If the convergence criterion is not met, the algorithm calculates a new

211   mass flow and returns to step 1. Otherwise the algorithm returns the solution.

212 Convergence criteria are written as absolute differences where the tolerances, i.e. ε_{th} and ε_{fd}, are set

213 to 10^{-3} °C and 10^{-2} Pa for the thermal and fluid-dynamic model respectively. The heat transfer and

214 pressure drop correlations presented in [28] were used for the calculations and are briefly summarized

215 below.

216 The water internal heat transfer coefficient in the economizer and in the superheater are calculated

217 with the Dittus-Boelter [29] and the Heinemen correlation [30] respectively. In formulas:

218 $$Nu_{ec,w} = 0.023\,\mathrm{Re}^{0.8}\,\mathrm{Pr}^{0.4} \quad (3)$$

219 $$Nu_{sh,w} = 0.133\,\mathrm{Re}^{0.84}\,\mathrm{Pr}^{0.333} \quad\quad\quad (4)$$

220 In the evaporating section, the Chen correlation [31] was used to calculate the heat transfer

221 coefficient:

222 $$\alpha_{ev,w} = \alpha_{bl}S + \alpha_{ls}F \quad\quad\quad (5)$$

223 where the suppression factor S accounts for the reduction of the boiling heat transfer coefficient when

224 convective boiling becomes dominant; F is the Chen phase multiplicator. For further details the reader

225 is referred to the original work of Chen [31].

226 On the molten salts side, the steam generator can be modeled as a bank of helicoidal tubes in cross-

227 flow. The Nusselt number was calculated combining a turbulent and a laminar term in the following

228 way [30]:

229 $$Nu_{MS} = 0.3 + \sqrt{Nu_{lam}^2 + Nu_{turb}^2} \quad\quad\quad (6)$$

230 where:

231 ○ $$Nu_{lam} = 0.664\sqrt{\mathrm{Re}}\,\mathrm{Pr}^{\frac{1}{3}} \quad\quad\quad (7)$$

232 ○ $$Nu_{turb} = \frac{0.037\,\mathrm{Re}^{0.8}\,\mathrm{Pr}}{1 + 2.433\,\mathrm{Re}^{-0.1}\left(\mathrm{Pr}^{\frac{2}{3}} - 1\right)} \quad\quad\quad (8)$$

233 Once the internal and external heat transfer coefficients, i.e. α_i and α_o, are known the global heat

234 transfer coefficient of the j-th volume U_j is obtained as:

235 $$U_j = \left(\frac{1}{\alpha_i} + \frac{r_i}{r_o\,\alpha_o} + \frac{r_i\log\left(\frac{r_o}{r_i}\right)}{k_t}\right) - 1 \quad\quad\quad (9)$$

236 The heat transfer rate exchanged in the j-th volume $\dot{Q}_j$ is hence calculated as follows:

237 $$\dot{Q}_j = U_j S_j (T_{FW_j} - T_{MS_j}) \quad\quad\quad (10)$$

238 The temperature profiles on the water and molten salts side are then calculated according to an upwind

239 scheme. For the economizer and superheater sections we write:

240 $$T_{FW_{j+1}} = T_{FW_{j+1}} - \frac{\dot{Q}_j}{m_{FW}c_{p,FW}} \quad\quad\quad (11)$$

241 In the evaporating section, the water temperature is always equal to the saturation temperature and

242 we monitor the evolution of the vapor fraction x_{FW} as following:

243 $$x_{FW_{j+1}} = x_{FW_j} + \frac{\dot{Q}_j}{m_{FW}h_{fg}} \quad\quad\quad (12)$$

244 On the molten salts side we have:

245   $$T_{MS_{j+1}} = T_{MS_{j+1}} - \frac{\dot{Q}_j}{m_{MS}c_{p,MS}}$$ (13)

246   The correlations for a bank of helicoidal tubes in cross flow proposed in [30] are used for fluid-

247   dynamic calculations. After the preliminary calculation of the geometrical factor k_1, the Euler number

248   Eu is obtained as follows:

249   $$\frac{Eu}{k_1} = 0.263 + \frac{0.867 \cdot 10^{-2}}{Re} - \frac{2.02}{Re^2} \qquad \text{for} \quad Re < 2 \cdot 10^3$$ (14)

250   $$\frac{Eu}{k_1} = 0.235 + \frac{0.198 \cdot 10^{-4}}{Re} - \frac{0.124 \cdot 10^{8}}{Re^2} + \frac{0.312 \cdot 10^{11}}{Re^3} - \frac{0.274 \cdot 10^{14}}{Re^4} \quad \text{for} \quad 2 \cdot 10^3 \leq Re < 2 \cdot 10^6$$

251   (15)

252   As far as the modeling of the stratification in the TES is concerned, we consider the Reynolds-

253   averaged version of the turbulent Navier-Stokes equations. Mathematically:

254   $$\frac{\partial \rho}{\partial t} + \frac{\partial \rho u_j}{\partial x_j} = 0$$ (16)

255   $$\frac{\partial \rho u_i}{\partial t} + \frac{\partial}{\partial x_j}(\rho\, u_j u_i) = -\frac{\partial P}{\partial x_i} + \frac{\partial \sigma_{ij}}{\partial x_j} + F_i$$ (17)

256   $$\frac{\partial \rho E}{\partial t} + \frac{\partial}{\partial x_j}(\rho u_j H) = \frac{\partial}{\partial x_j}(u_i \sigma_{ij}) - \frac{\partial}{\partial x_j}\left(\left(\frac{\mu}{PR} + \frac{\mu_T}{PR_t}\right)\left(\frac{\partial T}{\partial x_j}\right)\right)$$ (18)

257   where σ_{ij} is the tensor of viscous stresses, S_{ij} is the tensor of shear stresses and H is the total

258   enthalpy. Closure of the turbulent equations is provided through a $k - \omega$ model.

259   The governing equations are converted to algebraic equations using the finite-elements method in

260   COMSOL Multiphysics [32] with 2nd order Lagrange finite elements for the velocity field and linear

261   elements for the pressure and temperature fields. Time integration lies on a fully-implicit variable-

262   order variable-time step BDF (Backward Differentiation Formula) scheme with maximum and

263   minimum order set to 5 and 2 respectively. The time step is accepted if the L_2 norm of a predictor-

264   based relative error estimates is below 1e-3. The set of nonlinear equations arising from the spatial

265   and temporal discretization are solved via the under-relaxed Newton method. Preliminary numerical

266   experiments have shown that setting the under-relaxation factor to 0.85 is a good trade-off between

267   reliable convergence and computational cost. Convergence is considered satisfactory when the L_2

268   norm of the residuals drops below 1e-6. At each Newton iteration, the system of linearized equations

269   is solved via the MUltifrontal Massively Parallel Sparse direct Solver (MUMPS) [33]. Verification

270   has been performed with a-posteriori error estimates based on the use of the Richardson extrapolation

271   [34]. A free-triangular mesh with 4.1e4 elements has been chosen as the one that guarantees a Grid

272   Convergence Index (GCI) [35] below 1 %. The element size in the axial direction is 0.5 cm while in

273   the radial direction is 1.5 cm

274 The CFD approach is too demanding for system-level simulations. Hence, in this paper we use a

275 logistic distribution function to represent the non-dimensional molten salts temperature profile of a

276 vertical fluid column inside the tank. The function was parametrized statistically, using 18

277 Computational Fluid-Dynamic (CFD) simulations. This approach proved to be extremely convenient

278 for the adaptation of CFD results to annual system-level simulation and optimization. For an extensive

279 discussion on the reduction methodology, the reader is referred to [36]

280 *3.2.2 Experimental validation*

281 Figure 6(a) shows the results for the steam generator operated with 85 % of the nominal mass flow

282 rate (0.11 kg/s) of water and for a molten salts inlet temperature of 520 °C. The molten salts side

283 results show very good agreement with experimental data. The skin temperature (i.e. metal

284 temperature of the external surface of the receiver tube) calculation is quite accurate in the

285 evaporating section while it shows a non-negligible deviation in the superheating section. However,

286 the trend is well reproduced and the large error is mainly due to the sharp increase of the water

287 temperature in the superheating section. A small difference of the water mass flow, in fact, can result

288 in large relative errors.

289 Figure 6.(b) and Figure 6.(c) show the results obtained with a water mass flow 10 % and 20 % higher

290 than the nominal value. Differently from the previous case, the water side is quite well approximated

291 except for the top section of the steam generator

292 In all the tests conducted we obtained an average absolute error in the molten salts temperature of

293 3.16 °C with a standard deviation of 3.22 °C. Furthermore, an excellent agreement between predicted

294 and experimental inlet/outlet temperatures of water and molten salts is achieved, thus the model can

295 be confidently used for system-level simulations.

296 The validation of the CFD model is an essential step of the methodology proposed in the present

297 paper, allowing to proceed with multiple simulations in different conditions and to characterize the

298 reduced model (i.e. the logistic function) by statistical means. Validation has been performed using

299 experimental data taken from 14 thermocouples equally spaced every 10 cm on a long rod that is

300 immersed vertically in the tank at r = 0.5 m.

301 The validation of the discharging process is shown in Figure 7(a). Solid lines are the results obtained

302 by the CFD simulation, while starred indicators are the experimental data. The average absolute error

303 is 1.18 °C with a standard deviation of 2.53 °C. As far as the standby process is concerned, the results

304 are compared for a total period of approximately 27.8 hours. Referring to Figure 7(b), starred red

305 markers indicate the experimental results, while blue solid lines are obtained by the CFD simulation

306 A very good agreement is reached in the upper part of the tank where the rate of temperature drop in

307 time is perfectly predicted by the CFD model. Also in this case, the comparison with experimental

308 data is satisfactory with an average absolute error if 1.91 °C and a standard deviation of 3.14 °C.

309 The reduced model was then tested against the CFD simulations to verify its accuracy. The prediction

310 achieved through the two modeling approaches are compared in Figure 8 for both a charging and a

311 discharging process. The results obtained with the reduced model show a nearly perfect agreement

312 with the CFD ones. The interested reader is advised to examine [36], for the full details and the

313 potential applications of this model reduction approach.

314 **3.3 Power block**

315 The power block sub-system includes three main components: the steam turbine, the steam condenser

316 and the feedwater pump.

317 The thermodynamic performance of the steam turbine is modelled according to Medina Flores et al.

318 [37]. The Authors proposed to write the isoentropic efficiency of the turbine as a function of the steam

319 pressure at the inlet and at the outlet section of the turbine.

320 In summary, the electrical power output can be written as:

321 $$\dot{E}_{el} = \frac{1}{\beta}\left(\dot{m}\left(h_1 - h_{2,iso}\right) - \alpha\right) \tag{19}$$

322 where α and β are two pressure-dependent fitting parameters calculated as proposed in the original

323 reference.

324 According to Ref. [37], the power output of the turbine during the startup can be obtained through

325 the use of a startup factor $F_{startup}$ in the following way:

326 $$\dot{E}_{el} = F_{startup}(t)\dot{E}_{nom} \tag{20}$$

327 The correction factor ranges from 0 to 1, at the beginning and at the end of the startup process

328 respectively, and increases quadratically in time. It can be calculated with:

329 $$F_{startup}(t) = \left(\frac{t_{\sin ceStartup}(t)}{t_{startup}}\right)^2 \tag{21}$$

330 In the framework of this paper, $t_{startup}$ is set to one hour.

331 The condenser considered in the present work is a shell-and-tube heat exchanger as the one described

332 in Ref. [38]. Its axial coordinate is discretized and in each of the volume considered, the thermal

333 power $\dot{Q}$ is calculated by means of an energy balance.

334 The global heat transfer coefficient is determined as follows [38]:

335 $$U = \left(R_{fo} + \left(\frac{1}{\alpha_i} + R_{fi}\right)\frac{d_o}{d_i} + \frac{th_t}{k_t}\frac{d_o}{D_m} + \frac{1}{h_o}\right)^{-1} \tag{22}$$

336 Here, R_{fi} is the fouling factor, d is the diameter, th_t is the tube thickness, k_t is the tube conductivity

337 and α is the heat transfer coefficient. Subscripts i and o apply for internal and external side of the

338 tube respectively. D_m is the mean diameter calculated as follows:

339
$$D_m = \frac{d_o - d_i}{\ln\left(\frac{d_o}{d_i}\right)} \tag{23}$$

340 Moving to the feedwater pump, the approach followed is the one of Pelster [39], where the power

341 consumption of the device $\dot{E}_{pump}$ is calculated with:

342
$$\dot{E}_{pump} = \frac{1}{\eta_h} \dot{m}_{FW}\left(\frac{\Delta p}{\rho}\right) \tag{24}$$

343 Following the approach proposed by the same author, the pump outlet temperature T_{out} is computed

344 as [38]:

345
$$T_{out} = T_{in} + \frac{(1 - \eta_h)\dot{E}_{pump}}{\dot{m}\bar{c}_p} \tag{25}$$

346 Due to the high degree of maturity of these conventional components, the power block model is

347 considered reliable enough, and in this case, no experimental validation is performed.

348 **4   Cases considered**

349

350 In this paper, two different optimization cases are considered:

351 - CASE 1: THE MODULAR DESIGN: which has the aim of showing the potential of the

352   technology and the advantages of cogeneration in a deliberately general setup

353 - CASE 2: THE TAILORED DESIGN, which has the aim of demonstrating the

354   competitiveness of the technology in a specific market with real thermal users.

355 The modular design is a single-objective optimization of the system configuration in order to

356 minimize the Levelized Cost of Electricity. In this case, we fix the size of the plant to 1 MW$_e$, which

357 should fit many mid-size industrial users and we consider the system to be located in Rome. As far

358 as cogeneration is concerned, since the objective of this case is to quantify the maximum economic

359 advantages that cogeneration can bring, we consider an ideal thermal load where waste heat is always

360 fully utilized to satisfy heating and cooling needs.

361 On the other hand, the tailored design is a double objective optimization built to minimize the payback

362 time and to maximize the fraction of user's heating and cooling load satisfied by the solar system, i.e.

363 the Thermal Load Capacity Factor (TLCF). Hence, in this case, we consider both a real thermal load

364 and a real power market. The user in question is a 500 beds hospital, located in middle-Italy. The

365 name of the hospital cannot be revealed due to non-disclosure agreements. The heating load is

366 completely satisfied by a simple natural gas boiler while cooling is obtained through a hybrid system

367 where vapor compression chillers are used for base load and gas absorption chillers are used for peak

368 shaving and security of supply. The absorption machines are single-effect water-LiBr chillers. Their

369 operation is modeled with a constant COP of 60 %, as suggested in [23] for this type of machines.

370 Since the cooling system is already in place and its installation is rather recent (dated 2013), we do

371 not account for it in our economic analysis.

372 The fraction of the building thermal load satisfied through natural gas is monitored through hourly

373 readings of the meter. Figure 9(a) and 9(b) show the thermal load on a typical winter day and on a

374 typical summer day respectively. These graphs are obtained by averaging the measurements over the

375 season considered. In winter, two load peaks are visible, one in the morning around 7 am and one at

376 night around 8 pm. The load is much steadier in summer where only small fluctuations are visible

377 between 1 pm and 8 pm. The cumulative power distribution in the year considered is given in Figure

378 9(c). A base load is well identified to be slightly more than 500 kW and the peak demand is roughly

379 2500 kW.

380 Compared to Case 1, the tailored design should include two additional design variables:

381 • The size of the power plant, which should fit the specific needs of the user

382 • The size of a hot water storage tank, which is needed to handle successfully possible
383 mismatches between power block operations and the heating/cooling load

384 The building is located in a slightly populated area, with large ground availability for the installation

385 of the solar field. The vicinity of the solar field makes the distribution thermal losses negligible.

386 **5   Optimization setup**

387 Evolutionary algorithms are acknowledged to be the most suitable choice for the optimization of

388 complex energy systems, which often result in Mixed Integer highly Non-Linear Problems (MINLPs)

389 with several non-feasible holes in the design space [40].

390 In this paper, we use the parallel implementation of the GA of the MATLAB Optimization Toolbox

391 with a total of 10 decision variables (summarized in Table 1) and a population size of 50 individuals.

392 The initial population is randomly generated in the feasible region.

393 Convergence is considered reached when the average L_2 norm step in the normalized objective(s)

394 space drops below 1e-2. This happened after a total of 52 and 62 generations for the 1st and 2nd case

395 respectively.

396 The design variables are selected to enhance freedom in the design of the most relevant power plant

397 components, i.e. the TES, the power block, the solar field, the steam generator and the waste heat

398 utilization system.

399   Starting from the TES, the number of storage hours NH is an intuitive representation of the storage

400   tank size. This value is the number of hours of continuous nominal operation that could be guaranteed

401   to the power block during an ideal discharge process, i.e. starting from the tank fully charged at the

402   maximum temperature and assuming no mixing or diffusion during the discharge. The aspect ratio of

403   the tank is defined as the ratio of the tank diameter D to the tank height H and its choice is the trade-

404   off between two competing phenomena: a large tank aspect ratio brings a small average Reynolds

405   number of the molten salts during the charging and discharging phase which reduces thermocline

406   degradation due to turbulence effects. On the other hand, a small tank aspect ratio, although reducing

407   the area of contact with the cold and the hot fluid, brings more turbulent degradation.

408   We chose the design turbine power P_e as the representative variable for the power block. Once P_e is

409   set, the remaining power block components are sized according to the design thermodynamic cycle

410   obtainable through the assumptions outlined in Section 2.2.

411   Moving to the solar field, the solar multiple (SM) is defined as the ratio of the total mirror area to the

412   "exact mirror area". This last quantity is the solar field aperture area required to deliver to the power

413   cycle the thermal power needed to operate the turbine in nominal conditions. Besides the total area,

414   the optimal number of collectors per string n_{coll} should also be carefully identified: this design variable

415   affects the average heat transfer fluid velocity, whose value is a tradeoff between heat transfer

416   efficiency and pressure losses. Moreover, the orientation of the solar field is expected to play a major

417   role on the annual performance of the system. The optimizer can vary this variable between 1 and 2,

418   being the former the N-S orientation and the latter the E-W orientation. Finally, the solar field design

419   has one more degree of freedom, the solar field spacing $d_{spacing}$ between adjacent strings of solar

420   collectors. A too compact solar field design can yield a high self-shadowing effect between solar

421   collectors and a consequent drop in the optical efficiency. On the other hand, a too far placement

422   implicates a higher land cost.

423   Two design variables were identified for the steam generator: the number of tubes n_{tubes} and the height

424   H. The bounds have been set according to some preliminary design performed by ENEA in the

425   framework of the OPTS European project [41].

426   In Case 2 we decided to evaluate the installation of a hot water storage tank placed right after the

427   condenser. Hence, a new design variable was created that is the water storage capacity quantified in

428   terms of full load hours NH_{water} of the heating/cooling system. This quantity is defined as the number

429   of hours of continuous operation guaranteed to the heating and cooling systems at maximum load.

430   As far as the objective functions are concerned, we consider:

431   • The Levelized Electricity Cost (LEC) for Case 1

432   • The Simple Pay-Back Time (SPBT) for Case 2

433   • The Thermal Load Capacity Factor (TLCF) for Case 2

434 The LEC was preferred over other economic indicators, e.g. the Net Present Value (NPV), for its

435 great adoption in the field of CSP, hence making comparison with other studies straightforward. Also

436 please note that the plant operator and the thermal user are considered two different entities in this

437 study, hence any purchase for the electrical grid or consumption of back-up natural gas by the latter

438 is disregarded.

439 The first two objectives, i.e. the ones accounting for the economic performance of the plant, are

440 defined as:

441 $$LEC = \frac{CRF \cdot C_{inv} + C_{y,O\&M} + C_{y,dec} + C_{y,cont} - R_{y,heat\&cold}}{E_y} \qquad (26)$$

442 $$SPBT = \frac{C_{inv}}{R_{y,electricity} + R_{y,heat\&cold} - C_{y,O\&M} - C_{y,dec} - C_{y,cont}} \qquad (27)$$

443 where:

444   • CRF [-] is the annualization factor that can be computed as:

445 $$CRF = \frac{i(1+i)^n}{(1+i)^n - 1} + k_{ins} \qquad (28)$$

446   In the previous equation the interest rate i and insurance rate k_{ins} are set to 7 % and 2 %

447   respectively as suggested in Ref. [39].

448   • C_{inv} [$] is the investment cost of the plant obtained summing the investment costs of all the

449   components, i.e. $C_{inv} = \sum C_i$. The investment cost of the ith component C_i is calculated through

450   the use of cost functions, which stem from a best-fit on a wide range of market data and relate

451   the cost of component to a specific size parameter S_i. Mathematically [39]:

452 $$C_i = c_{ref} \left(\frac{S_i}{S_{ref}} \right)^n f_{M\&S} \qquad (29)$$

453   The adopted $f_{M\&S}$ index for the present study is the one of 2011 obtained from Ref. [42] and

454   set to 1546.5. The full reference data of c_{ref}, S_{ref}, and n for the power block is obtained by [39],

455   while the ones related to the solar field and the molten salts TES are gathered from [43]. The

456   characteristic dimensions, their reference value and the specific reference costs of the

457   components considered are listed in Table 2. The characteristic dimensions are obtained

458   directly from the definition of the design variables. For more details on the cost function

459   approach used to calculate the components investment costs, the reader is referred to [40, 48].

460

461 • $C_{y,O\&M}\left[\frac{\$}{\text{year}}\right]$ represents the Operation & Maintenance costs. We consider service contracts for

462 ground keeping, mirrors washing and water treatment, material maintenance for the

463 equipment and operation cost due to personnel. All the data obtained through [43] are

464 normalized on the plant electrical capacity to obtain a specific O&M cost.

465

466 • $C_{y,cont}\left[\frac{\$}{\text{year}}\right]$ and $C_{y,dec}\left[\frac{\$}{\text{year}}\right]$ refer to contingencies costs and decommissioning costs. In the

467 present paper we follow the approach presented in Ref. [39] and set them to 10 % and 5 %

468 respectively of the total project cost.

469

470 • $R_{y,heat\&cold}\left[\frac{\$}{\text{year}}\right]$ accounts for the revenues from the heat market considered as savings brought

471 by the CSP cogeneration installation with respect to a conventional natural gas boiler and a

472 H_2O-LiBr absorption chiller. In mathematical terms:

473
$$R_{y,heat\&cold} = p_{NG}\left(\frac{Q_{heat} + \dfrac{Q_{cold}}{COP_{ACU}}}{\eta_{boiler}}\right) = p_{NG}\frac{Q_{wasteHeat}}{\eta_{boiler}}$$

474 (30)
475 where the second equality sign holds only in case of complete sale of the plant waste heat on

476 the market, i.e. case 1. We set the thermal efficiency of the typical natural gas boiler η_{boiler} to

477 90%, and the price of natural gas p_{NG} equal to 10.087 €/GJ, that is the market price for

478 industrial users as set by the Italian Ministry of Development and Economic Resources [44].

479 • $R_{y,electricity}\left[\frac{\$}{\text{year}}\right]$ accounts for the revenues from the electricity market and it is calculated as:

480
$$R_{y,electricity} = p_e E \tag{31}$$

481 Where p_e is the price at which electricity is sold in the italian power market, which is

482 determined by summing the fixed incentive of the Feed-In-Tariff (FIT) scheme and the

483 liberalized price with which electricity producers are remunerated on the day-ahead market.

484 Those last data are obtained on the GME (Italian Electricity Market manager) website [45]

485 for the year 2014 while the incentive tariff is set according to the Italian Ministerial Decree

486 of 6 Jul. 2012 to 320 €/MWh [46] .

487 Table 2 summarizes the most relevant data implemented in the economic model. For a more

488 exhaustive breakdown at the component level, the reader is advised to consult [43].

489 The last objective function (i.e. TLCF) quantifies the performances of the CSP plant when used in

490 cogeneration mode. It is calculated as:

491 $$TLCF = 1 - \frac{E_{backup}}{Q_{heat} + Q_{cold}}$$ (32)

492 that is the solar fraction of the annual heating and cooling demand.

6 Results and discussion

6.1 Case 1

495 Table 3 presents the optimized design specifications for Case 1. The optimal design presents a high

496 value of solar multiple and storage tank size in order to increase the capacity factor of the steam

497 turbine. However, the optimal storage tank size and solar multiple are far from the upper bound set

498 for the optimization routine. This means that an optimum is present in the range considered and that

499 the marginal cost of adding storage capacity and more mirrors to the solar field does not pay off.

500 On the other hand, the number of collectors per string is maximum which means that increasing the

501 length of the single string results in a higher annual yield of the solar field.

502 The height of the steam generator and the number of tubes selected are in close agreement with the

503 preliminary design proposed by the manufacturer for the European Project OPTS. Finally, the optimal

504 tracking axis orientation found is N-S which brings an 11% increase in the annual electricity yield of

505 the unit square meter compared with E-W orientation.

506 The main annual energy flows and first-law efficiencies are summarized in Table 4. The proposed

507 system in the optimized configuration generates 3864 MWh of electricity per year, which results in a

508 capacity factor of the power block of 38.6 %.

509 The second-law analysis of the system in the optimized configuration is conducted to identify the

510 most critical components. A summary is presented in Table 5 while a representation of the exergy

511 streams in the CSP plant is given in Figure 10. The exergy efficiency for each component is calculated

512 as following [44]:

513 $$\eta = \frac{E_p}{E_f} = 1 - \frac{E_d + E_l}{E_f}$$ (33)

514 where E_p is the exergetic product of the component, E_f are the exergetic resources used to drive it,

515 E_d and E_l represent the exergy destruction and the exergy losses of the component.

516 Most of the solar exergy hitting the reflectors, i.e. 51.4 %, is lost before reaching the receiver tube

517 due to imperfect concentration. Another big portion is lost or destroyed in the receiver tube such that

518 only 23.3 % of the solar exergy reaches the storage unit. Hence, it is clear that the most critical

519 components are the solar-to-thermal converters. An effective strategy to increase the second-law

520 efficiency of the system is to adopt reflectors with higher optical efficiency and/or multiple axis

521 tracking. This would certainly modify the optimal design of the plant: the increased system products

522 yield per surface ratio would make a larger solar field convenient. On the other hand, most of the
523 exergy optimization studies consider the unit exergetic cost [49] of the functional products as the
524 performance measure of the plant. To this aim, the storage unit, which presents a higher exergetic
525 efficiency, can be improved by reducing the exergy destruction in the thermocline, as shown in [28].
526 Little room for improvement is left in a mature component like the power block.

527   Anyhow, the exergetic performance of the system is not considered in the optimization problem
528 formulation and further investigations on this matter are left to future extensions of this work.

529 The stratified storage has an acceptable exergetic efficiency, i.e. roughly 83 %. This figure of merit
530 allows for a performance comparison between single tank and double tank storage systems. The
531 exergy product of a storage unit can be written in the following form:

532 $$E_p = \rho_E V \eta \tag{34}$$

533 where ρ_E is the exergy density of the unit (MWh/m^3) and V is the total volume. If the double-tank
534 installation (denoted by the subscript DT) is designed to deliver the same exergy of the single-tank
535 installation (denoted by the subscript ST) we can estimate the required volume ratio as:

536 $$\frac{V_{DT}}{V_{ST}} = \frac{\rho_{ST}\eta_{ST}}{\rho_{DT}\eta_{DT}} \tag{35}$$

537 where $\rho_{ST}/\rho_{DT} = 2$. If we consider an ideal (i.e. with 2nd law efficiency equal to unity) double-tank
538 storage system we obtain $V_{DT}/V_{ST} = 1.67$. The additional investment cost of the double-tank
539 alternative results in a LEC of 272.59 $/MWh, which is 18 % higher than the one obtained with a
540 single-tank system.

541 Moving to the analysis of economic performances, the system requires a total capital investment of
542 14.56 million of US$ and can generate electrical power at the levelized cost of 230.25 $/MWh. From
543 a comparison with studies on Parabolic Through solar plants ([50-52]), where the estimated LEC
544 ranges from a minimum of 200 $/MWh to a maximum of 360 $/MWh for plants sizes in the range of
545 50 MW$_e$ to 100 MW$_e$, it is clear that the solution proposed has competitive economic performances.

546 The CAPital Expenditures (CAPEX) and LEC breakdown are represented in the pie charts of Figure
547 11. The cost of the solar field is still the major contributor to the total power plant investment cost
548 accounting for 54 % of the total. The second largest item in the plant's owner expenditures list is the
549 power block, which accounts for 15% of the total cost. Finally, the storage tank represents only 10 %
550 of the total cost in the optimized configuration. The other pie chart represents the Levelized Electricity
551 Cost breakdown where also the revenues generated from the heat sold on the market are included. In
552 this way, it is possible to notice that cogeneration has the potential to decrease the specific cost of
553 electricity of 28 % and this option is thus crucial for the economic viability of small CSP systems.

6.2 Case 2

554

555 Figure 12 presents the Pareto front obtained from the multi-objective optimization of Case 2. It can

556 be noticed that the minimum possible payback-time found is slightly higher than 6 years and the

557 maximum fraction of thermal load covered by the solar resource that can be reached is very close to

558 87 %. A complete thermal load coverage is extremely non-economical. In order to satisfy completely

559 the winter request, where the thermal load is maximum and the solar yield minimum, the system

560 would be oversized for most of the year and a large fraction of the thermal energy would not be

561 utilized nor remunerated. The hybridization of the heating and cooling system looks from the curve

562 the most interesting option.

563 Two extreme points are selected from the Pareto front and their annual performance is analyzed. Point

564 1 is the most economically viable solution, while the second design, i.e. Point 2, is the one that

565 guarantees the highest solar coverage of the heating and cooling load.

566 The design specifications and the techno-economic performance of the system in the two selected

567 points are summarized in Table 6. The first issue to notice is that in both points the tracking axis is

568 selected to be East-West oriented. It is well known that this orientation choice guarantees a steadier

569 output throughout the year compared to the N-S counterpart at the price of a lower yearly energy

570 yield. However, we found that the N-S orientation results in a high amount of thermal energy wasted

571 during summer months due to a solar generation that largely exceeds the demand.

572 The optimal combination of solar multiple, molten salts storage tank size and nominal power of the

573 steam turbine is very interesting. It is found, in fact, that is more convenient to buy a large steam

574 turbine coupled with a small tank at the cost of a low capacity factor rather than investing in a big

575 storage tank. On the other hand, there are no appreciable differences in the steam generator design

576 between the two Pareto points which confirms the observations of the previous optimization run. The

577 design of point 2 gives a total efficiency decrease of 2 %. The electrical capacity factor of the power

578 block is very similar in the two points and differences in the total electricity generation are mainly

579 due to a slight difference in the nominal steam turbine power selected for the optimal design.

580 The total investment cost of the design in Point 2 is roughly 3.5 M$ higher than the one in point 1.

581 The difference comes mainly from the solar field cost, from the molten salts storage tank cost and

582 from the water tank cost. The total cost breakdown in the two points is depicted in Figure 13. The

583 relative investment in storage technologies, i.e. water tank and Molten Salts storage tank is nearly 10

584 % higher for Point 2 than for point 1. A larger portion than expected is attributed to the purchase of

585 the hot water storage.

586 In order to investigate more in details the trends behind the solution found, the system is simulated

587 with different combinations of steam turbine and storage tank sizes. The turbine size is allowed to

588 vary between 1000 kW and 3000 kW with steps of 400 kW, while the tank storage size is allowed to

589 vary between 2 and 18 hours with steps of 4 hours for a total of 20 design points analyzed. The size

590 of the solar field, in terms of mirror area is fixed to 28000 m^2, as obtained for the design of Point 1.

591 The water tank size is set to a very small value, i.e. 2 hours, in order to exclude the influence of this

592 parameter on the system performance. All the other parameters are set equal to the design

593 specifications of Point 1.

594 In all the possible combinations obtained through this procedure, we analyze the normalized

595 breakdown of the power plant revenues, i.e. we consider:

- 596 • The incentive-related revenues per unit of investment, in the form of Feed-In-Tariff (FIT) due
- 597 to the amount of electricity generated
- 598 • The heat-related revenues per unit of investment, due to the heat sold to the user.
- 599 • The power market-related revenues per unit of investment, due to the selling of power to the
- 600 electrical grid.

601 The trend of the FIT-related specific annual revenues per unit of investment $\left[\frac{\$}{year\,\$_{inv}}\right]$ for different

602 combinations of the two decision variables selected is depicted in Figure 14.(a). If this was the only

603 earning source of the plant, most convenient designs would be obtained for small steam turbine sizes

604 with big storage tanks. However, by looking at Figure 14.(b), it is clear that specific revenues

605 connected to real market trends are greater for big turbines and for small storage tank size. The reason

606 for such a behavior is that those plants deliver a higher amount of energy right in the middle of the

607 day and thus the average price at which the power is sold is higher. Increasing the operating hours of

608 the steam turbine only adds cost to the system and lower the average price of electricity. As far as the

609 heat-related revenues are concerned (Figure 14(c)), turbine sizes in the range between 1600 kW and

610 2300 kW are recommended for the hospital considered because higher Thermal Load Capacity

611 Factors can be achieved.

612 This last analysis shows that the optimal system configuration may vary considerably depending on

613 the incentive policy framework in which the plant is operated.

614 **7 Conclusions**

615 In this paper, we firstly presented an efficient and flexible modeling framework that can accurately

616 predict the performance of the single storage tank with integrated steam generator. In particular, the

617 1D finite volume model of the steam generator predicts the molten salts temperature with a mean

618 absolute error of 3.16 °C, while the analytic approach used to reduce the CFD model of the tank can

619 reproduce the vertical temperature profile with a mean absolute error of 1.18 °C.

620 We used this validated model to optimize the system designs in two different cases. In the first case,

621 we optimized the design of a $1MW_e$ plant located in Rome with an ideal thermal load in order to

622 assess the potential of the technology for mid-size users. We revealed that this type of system could

623 generate power at a price of 230.25 $/MWh, if it is operated for 38 % of the year. In particular, the

624 possibility of utilizing locally the waste-heat, being responsible of a 28 % reduction of the Levelized

625 Cost of Electricity, is crucial for the economic viability of this kind of plants. Furthermore, we found

626 that the single tank configuration with integrated steam generator allows to decrease the specific

627 electricity of another 42 $/MWh compared to double tank option.

628 In the second case, we conducted a case-study with a 500 beds Italian hospital with the aim of

629 investigating the performances of the system with a real user in a real market framework. We found

630 that, if the system is properly designed, the investment costs can be recouped in a period between 6

631 and 7 years and a range between 80 % and 87 % of the heating and cooling demand can be satisfied

632 with the solar system.

633 **Acknowledgements**

637 **References**

638 [1] Lilliestam, J., Bielicki, J. M., & Patt, A. G. (2012). Comparing carbon capture and storage (CCS)

639 with concentrating solar power (CSP): Potentials, costs, risks, and barriers. Energy policy, 47,

640 447-455.

641 [2] W. Gaggioli and L. Rinaldi, "An Innovative Concept of a Thermal Energy Storage (TES) System

642 Based on the Single Tank Configuration Using Stratifying Molten Salts (MS) as both HSM and

643 HTF, and with an Integrated Steam," in SolarPACES international Conference 2013, 2014, pp.

644 780–789.

645 [3] C. Rubbia, "Solar Thermal Energy production: guidelines and future programmes of ENEA"

646 2001.

647 [4] Li, H., Huang, X., & Zhang, L. (2008). A lumped parameter dynamic model of the helical coiled

648 once-through steam generator with movable boundaries.Nuclear Engineering and Design,

649 238(7), 1657-1663

650 [5] Colorado, D., Papini, D., Hernández, J. A., Santini, L., & Ricotti, M. E. (2011). Development
651   and experimental validation of a computational model for a helically coiled steam
652   generator. International Journal of Thermal Sciences,50(4), 569-580.

653 [6] Dong, Z., Huang, X., Feng, J., & Zhang, L. (2009). Dynamic model for control system design and
654   simulation of a low temperature nuclear reactor. Nuclear Engineering and Design, 239(10), 2141-
655   2151.

656 [7] Flueckiger, S. M., Iverson, B. D., Garimella, S. V., & Pacheco, J. E. (2014). System-level
657   simulation of a solar power tower plant with thermocline thermal energy storage. Applied
658   Energy, 113, 86-96.

659 [8] Yang, Z., & Garimella, S. V. (2010). Thermal analysis of solar thermal energy storage in a molten-
660   salt thermocline. Solar energy, 84(6), 974-985.

661 [9] Strasser, M. N., & Selvam, R. P. (2014). A cost and performance comparison of packed bed and
662   structured thermocline thermal energy storage systems. Solar Energy, 108, 390-402.

663 [10] Nithyanandam, K., Pitchumani, R., & Mathur, A. (2014). Analysis of a latent thermocline storage
664   system with encapsulated phase change materials for concentrating solar power. Applied Energy,
665   113, 1446-1460.

666 [11] Fornarelli, F., Camporeale, S. M., Fortunato, B., Torresi, M., Oresta, P., Magliocchetti, L., ... &
667   Santo, G. (2016). CFD analysis of melting process in a shell-and-tube latent heat storage for
668   concentrated solar power plants. Applied Energy, 164, 711-722.

669 [12] Rivas, E., Rojas, E., Bayón, R., Gaggioli, W., Rinaldi, L., & Fabrizi, F. (2014). CFD model of a
670   molten salt tank with integrated steam generator. Energy Procedia, 49, 956-964.

671 [13] Palenzuela, P., Zaragoza, G., Alarcón, D., & Blanco, J. (2011). Simulation and evaluation of the
672   coupling of desalination units to parabolic-trough solar power plants in the Mediterranean region.
673   Desalination, 281, 379-387.

674 [14] Darwish, M. A., Abdul-Rahim, H., & Mohtar, R. (2012, October). Doha solar cogeneration
675   power desalting pilot plant: Preliminary design. In Qatar Foundation Annual Research Forum
676   (No. 2012).

677 [15] Ravaghi-Ardebili, Z., Manenti, F., Corbetta, M., Pirola, C., & Ranzi, E. (2015). Biomass
678   gasification using low-temperature solar-driven steam supply. Renewable Energy, 74, 671-680.

679 [16] Al-Sulaiman, F. A., Hamdullahpur, F., & Dincer, I. (2012). Performance assessment of a novel
680   system using parabolic trough solar collectors for combined cooling, heating, and power
681   production. Renewable Energy, 48, 161-172.

682 [17] Buck, R., & Friedmann, S. (2007). Solar-assisted small solar tower trigeneration
683   systems. Journal of Solar Energy Engineering, 129(4), 349-354.

684 [18] Chacartegui, R., de Escalona, J. M., Sánchez, D., Monje, B., & Sánchez, T. (2011). Alternative
685   cycles based on carbon dioxide for central receiver solar power plants. Applied Thermal
686   Engineering, 31(5), 872-879.

687 [19] Spelling, J., Favrat, D., Martin, A., & Augsburger, G. (2012). Thermoeconomic optimization of
688   a combined-cycle solar tower power plant. Energy, 41(1), 113-120.

689 [20] Silva, R., Berenguel, M., Pérez, M., & Fernández-Garcia, A. (2014). Thermo-economic design
690   optimization of parabolic trough solar plants for industrial process heat applications with
691   memetic algorithms. Applied Energy, 113, 603-614.

692 [21] Fiorenza, G., Sharma, V. K., & Braccio, G. (2003). Techno-economic evaluation of a solar
693   powered water desalination plant. Energy Conversion and Management, 44(14), 2217-2240.

694 [22] Falchetta, M., Gambarotta, A., Vaja, I., Cucumo, M., & Manfredi, C. (2006). Modelling and
695   simulation of the thermo and fluid dynamics of the "Archimede Project" solar power station. In
696   Proceedings of ECOS 2006.

697 [23] Srikhirin, P., Aphornratana, S., & Chungpaibulpatana, S. (2001). A review of absorption
698   refrigeration technologies. Renewable and sustainable energy reviews, 5(4), 343-372.

699 [24] F. Zaversky, R. Medina, J. García-Barberena, M. Sánchez, and D. Astrain, "Object-oriented
700   modeling for the transient performance simulation of parabolic trough collectors using molten
701   salt as heat transfer fluid," Sol. Energy, vol. 95, pp. 192–215, Sep. 2013.

702 [25] R. Forristall, "Heat Transfer Analysis and Modeling of a Parabolic Trough Solar Receiver
703   Implemented in Engineering Equation Solver Heat Transfer Analysis and Modeling of a
704   Parabolic Trough Solar Receiver Implemented in Engineering Equation Solver," Tech. Report,
705   Golden, Colorado, 2003.

706 [26] Retrieved May 23, 2014, from http://www.soda-is.com/eng/helioclim/helioclim3_eng.html

707 [27] Retrieved May 23, 2014, from https://energyplus.net/weather

708 [28] Pizzolato, A., Verda, V., & Sciacovelli, A.. Local entropy generation analysis of transient
709   processes – an innovative approach for the design improvement of a Thermal Energy Storage
710   with Integrated Steam Generator. Constructal Law & Second Law Conference 2015 CLC 2015,
711   Parma (Italy), 18-19 May.

712 [29] Dittus, F. W., & Boelter, L. M. K. (1985). Heat transfer in automobile radiators of the tubular
713   type. International Communications in Heat and Mass Transfer,12(1), 3-22.

714 [30] Kuppan, T. (2000). Heat exchanger design handbook (Vol. 126). New York: Marcel Dekker.

715 [31] Chen, J. C. (1966). Correlation for boiling heat transfer to saturated fluids in convective flow.
716   Industrial & Engineering Chemistry Process Design and Development, 5(3), 322-329. 25

717 [32] COMSOL, version 5.0, COMSOL Inc., Burlington, MA, USA, 2014.

718 [33] Amestoy, P. R., Duff, I. S., & L'Excellent, J. Y. (1998). MUMPS multifrontal massively parallel
719   solver version 2.

720 [34] Oberkampf, W. L., Trucano, T. G., & Hirsch, C. (2004). Verification, validation, and predictive
721   capability in computational engineering and physics. Applied Mechanics Reviews, 57(5), 345-
722   384.

723 [35] Roache, P. J. (1994). Perspective: a method for uniform reporting of grid refinement studies.
724   Transactions-American Society of Mechanical Engineers Journal of Fluids Engineering, 116,
725   405-405.

726 [36] Pizzolato, A., Donato, F., Verda, V., & Santarelli, M. (2015). CFD-based reduced model for the
727   simulation of thermocline thermal energy storage systems. Applied Thermal Engineering, 76,
728   391-399.

729 [37] J. M. Medina-Flores and M. Picón-Núñez, "Modelling the power production of single and
730   multiple extraction steam turbines," Chem. Eng. Sci., vol. 65, no. 9, pp. 2811–2820, May 2010.

731 [38] H. Hajabdollahi, P. Ahmadi, and I. Dincer, "Thermoeconomic optimization of a shell and tube
732   condenser using both genetic algorithm and particle swarm," Int. J. Refrig., vol. 34, no. 4, pp.
733   1066–1076, Jun. 2011.

734 [39] S. Pelster, D. Favrat, and M. R. von Spakovsky, "The Thermoeconomic and Environomic
735   Modeling and Optimization of the Synthesis, Design, and Operation of Combined Cycles With
736   Advanced Options," J. Eng. Gas Turbines Power, vol. 123, no. 4, p. 717, 2001

737 [40] Spelling, J. (2013). Hybrid Solar Gas-Turbine Power Plants: A Thermoeconomic Analysis, PhD.
738   thesis, Royal Institute of Technology (KTH), Stockholm

739 [41] Retrieved May 23, 2014, from http://www.opts.enea.it/

740 [42] M. Darwish (2012), "Modular Hybridization of Solar Thermal Power Plants For Developing
741   Nations," M.S. thesis, Royal Institute of Technology (KTH), Stockholm, 2012.

742 [43] Turchi, C. (2010). Parabolic trough reference plant for cost modeling with the solar advisor
743   model (SAM) (No. NREL/TP-550-47605). National Renewable Energy Laboratory (NREL),
744   Golden, CO.

745 [44] Retrieved October 10,2015, from http://dgsaie.mise.gov.it/dgerm/prezzigas.asp

746 [45] Retrieved October 10, 2015, from http://www.mercatoelettrico.org/en/

747 [46] Solar thermodynamic. Retrieved October 12, 2015, from http://www.gse.it/en/feedintariff/

748 [47] Technology data for energy plants Retrieved June 6, 14, from Energynet.dk

749 [48] Bejan, A., & Tsatsaronis, G. (1996). Thermal design and optimization. John Wiley & Sons.

750 [49] Lozano, M. A., and A. Valero. "Theory of the exergetic cost." Energy 18.9 (1993): 939-960.

751 [50] Hinkley, J. T., Hayward, J. A., Curtin, B., Wonhas, A., Boyd, R., Grima, C., & Naicker, K.
752   (2013). An analysis of the costs and opportunities for concentrating solar power in
753   Australia. Renewable energy, 57, 653-661.
754 [51] Kutscher, C., Mehos, M., Turchi, C., Glatzmaier, G., & Moss, T. (2010). Line-focus solar power
755   plant cost reduction plan. Contract, 303, 275-3000.
756 [52] International Energy Agency, "Technology Roadmap: Concentrating Solar Power," OECD
757   Publishing, May 2010
758
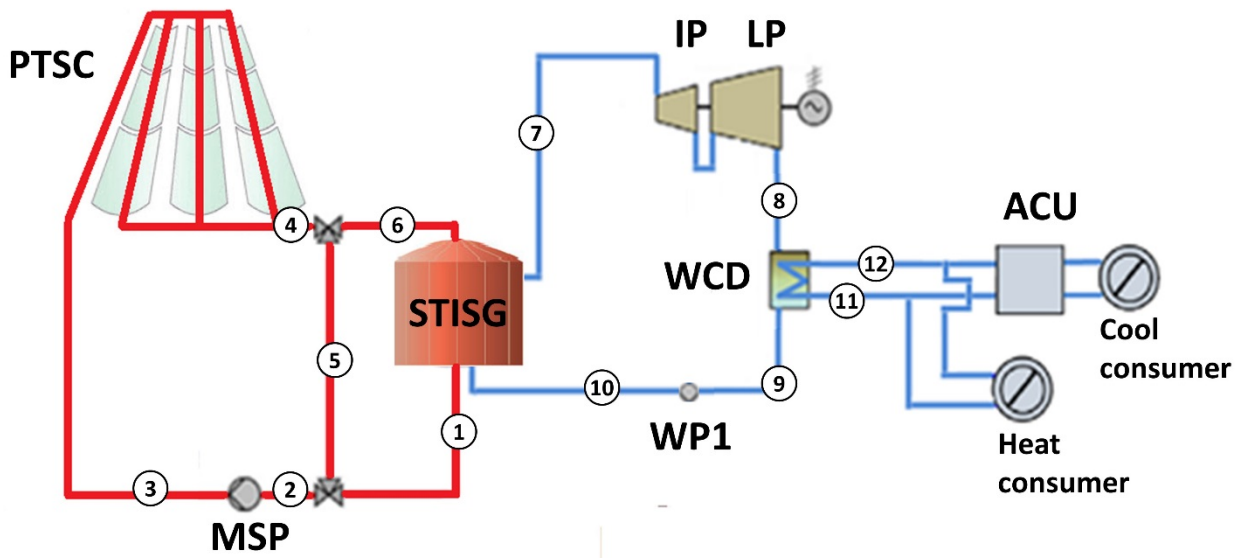
Figure 1. Proposed system layout

762
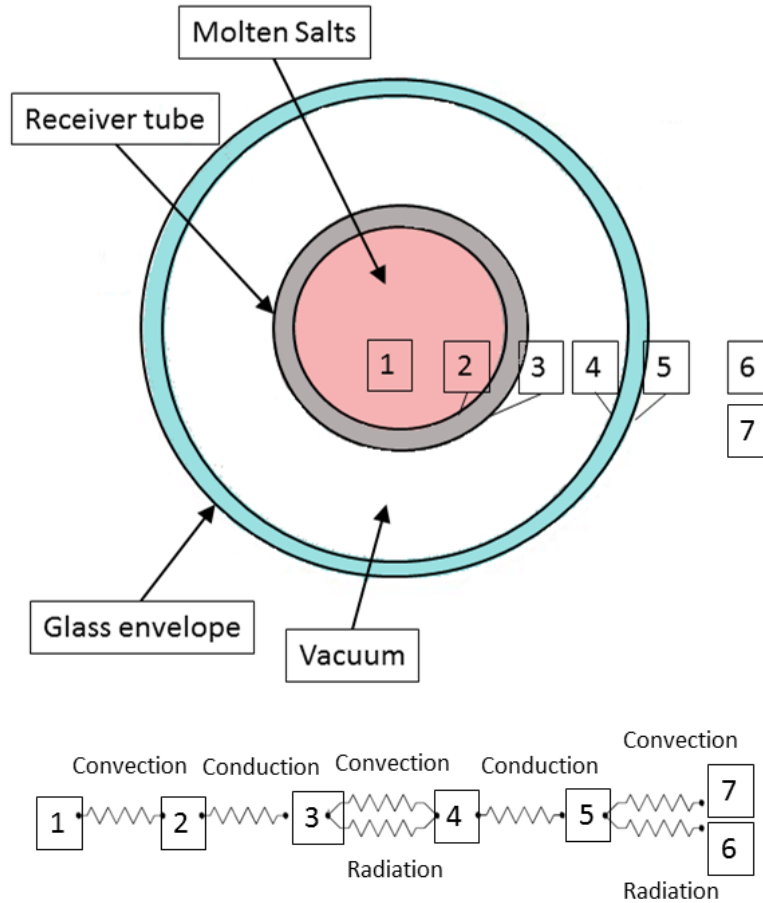
763
764 **Figure 2. Electrical analogy used to model the heat losses in the receiver tube [22]. (1) Heat Transfer Fluid, (2) absorber inner**
765 **surface, (3) absorber outer surface, (4) glass envelope inner surface, (5) glass envelope outer surface, (6) air, (7) sky.**
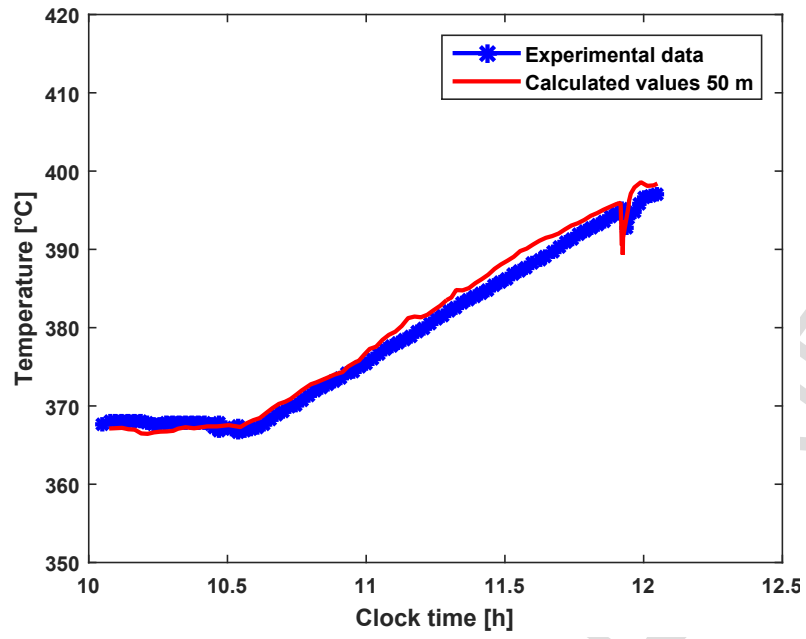
766

767

768 **Figure 3. Validation of the solar field model at ENEA Research Center La Casaccia.**

769

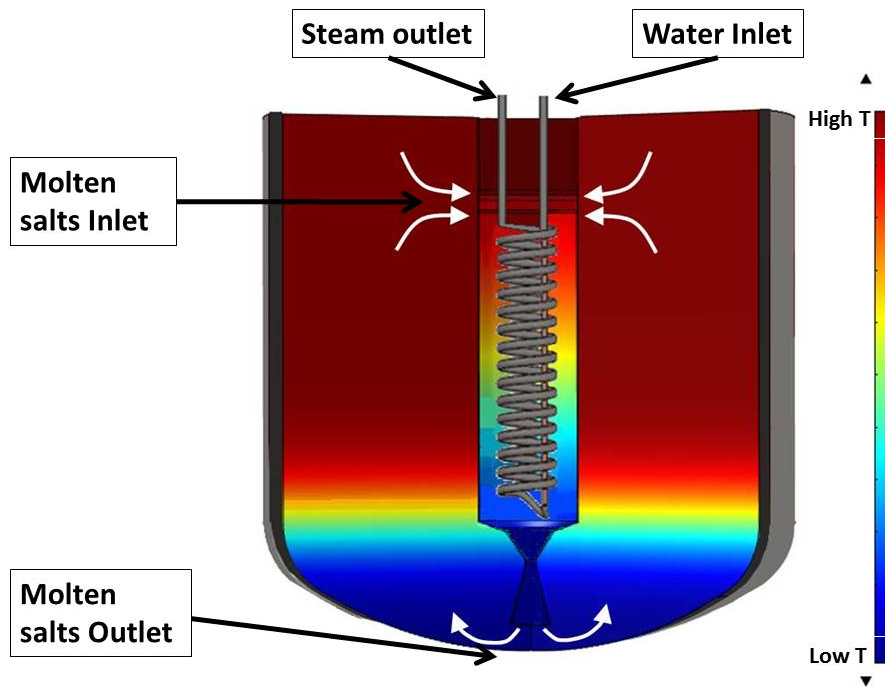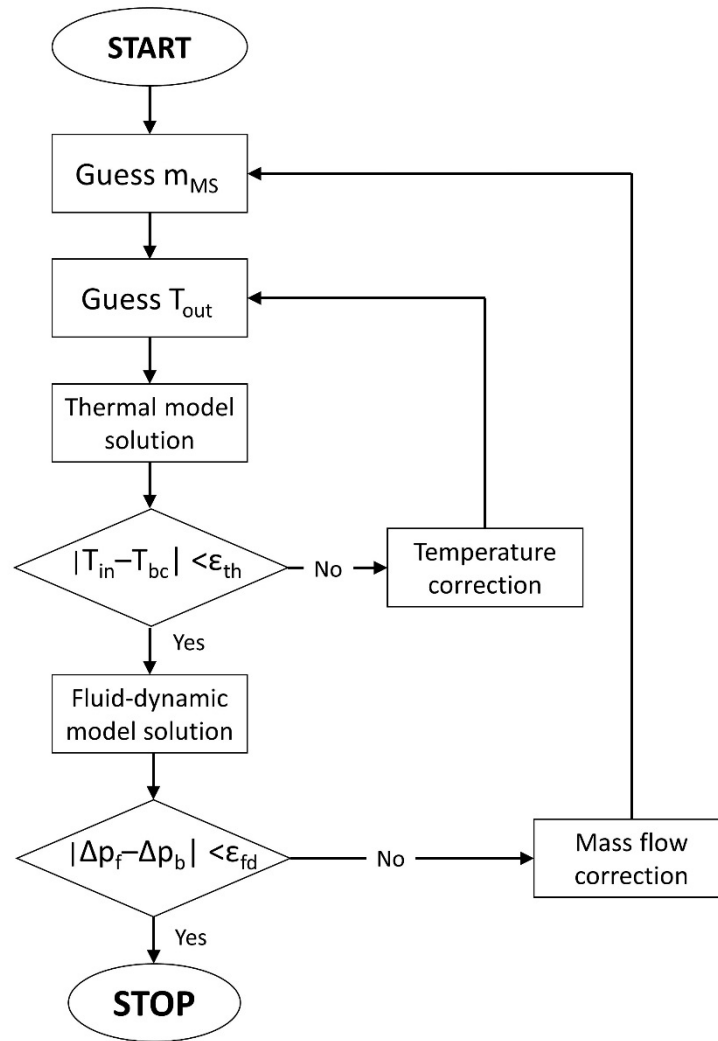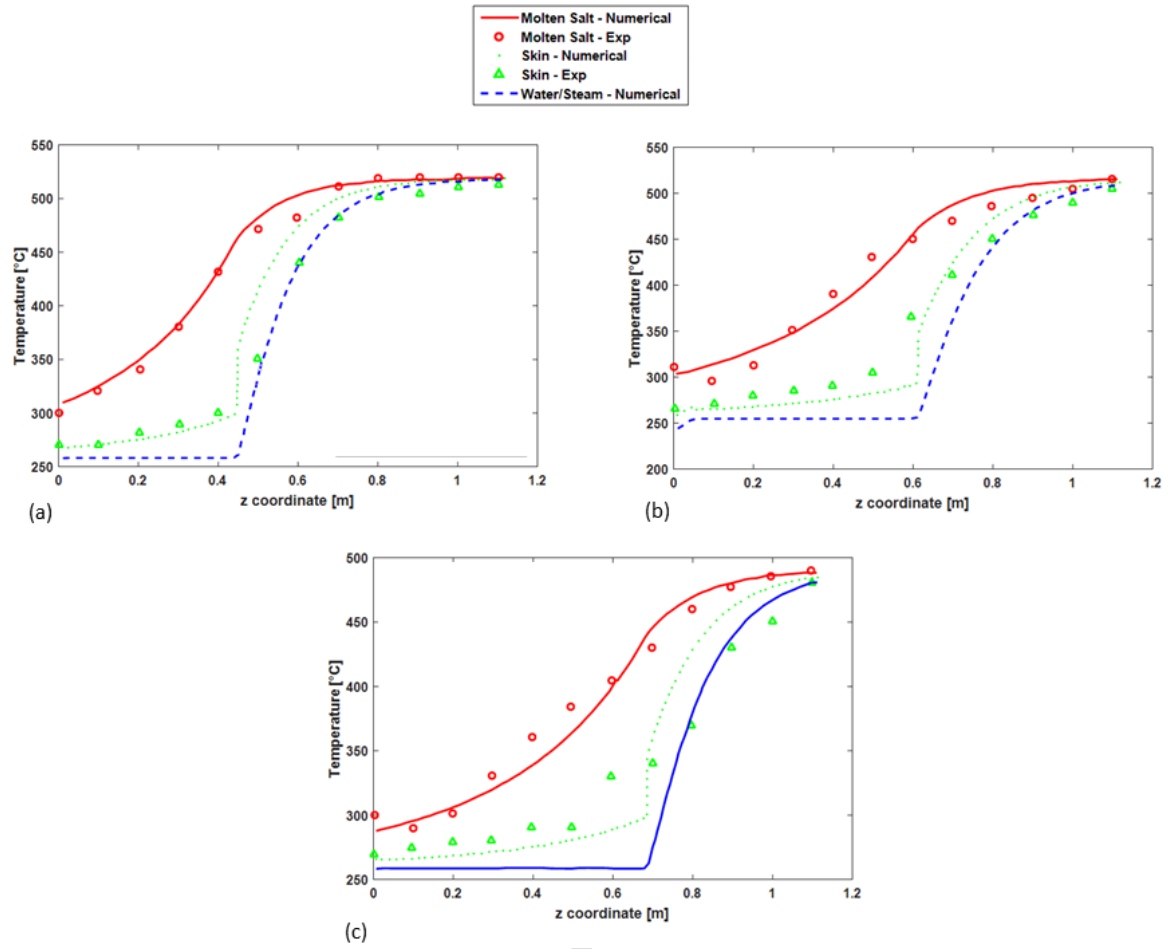**Figure 4. Schematics of the Thermocline TES with integrated Steam Generator**

773

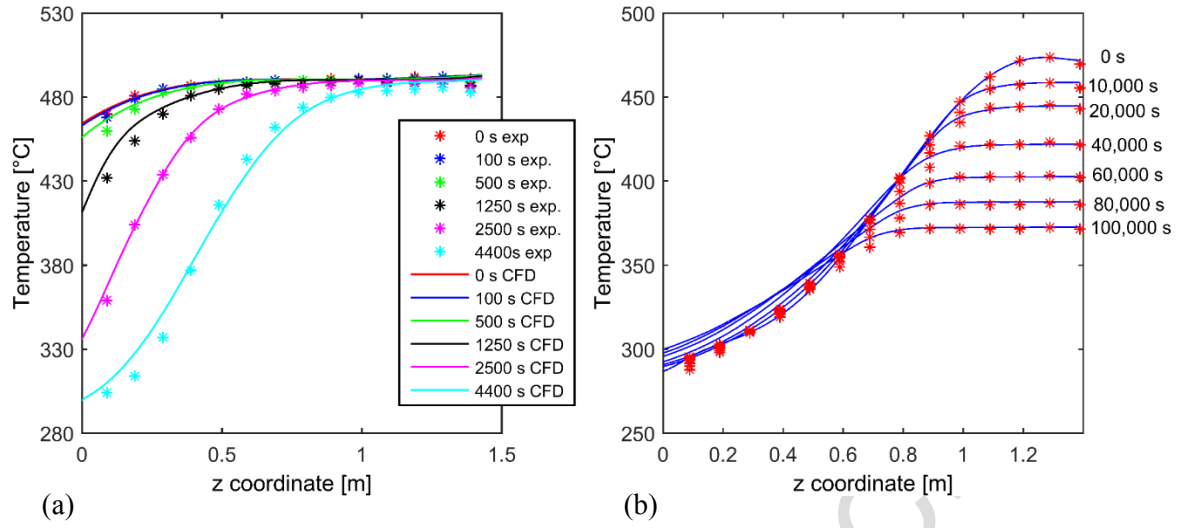774   **Figure 5. Computational model flow chart of the naturally-circulated steam generator**

775

776

Figure 6. Experimental validation of the steam generator model in three different conditions. (a): 520 °C, 45 bar, mass flow 85% of nominal. (b): 520 °C, 40 bar, mass flow 110% of nominal. (c): 480 °C, 46 bar, mass flow 120 % of nominal
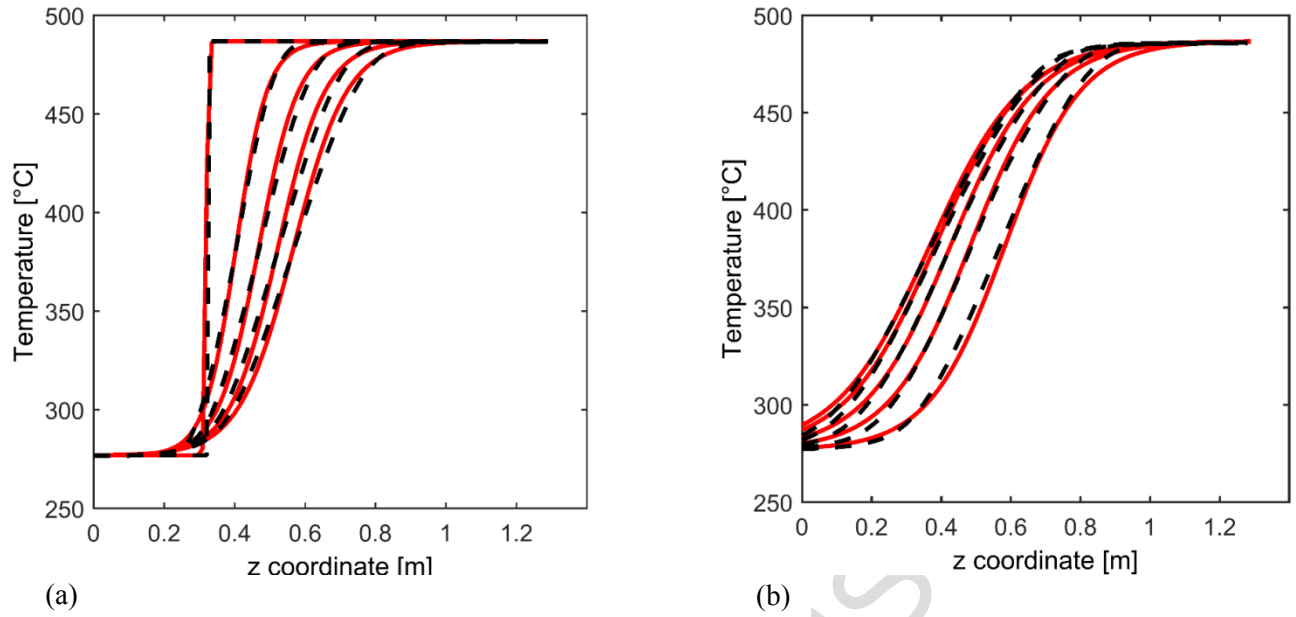
779

**Figure 7. Experimental validation of the CFD model of the storage tank. (a): charging; (b): standby.**

(a)

(b)

783

Figure 8. Validation of the reduced model for a continuous process with charging (a) and subsequent discharging (b) Red solid lines are the temperatures profiles obtained through the reduced model while black dotted lines are the ones obtained with the full CFD model [27].

787

788　(a)　(b)　(c)
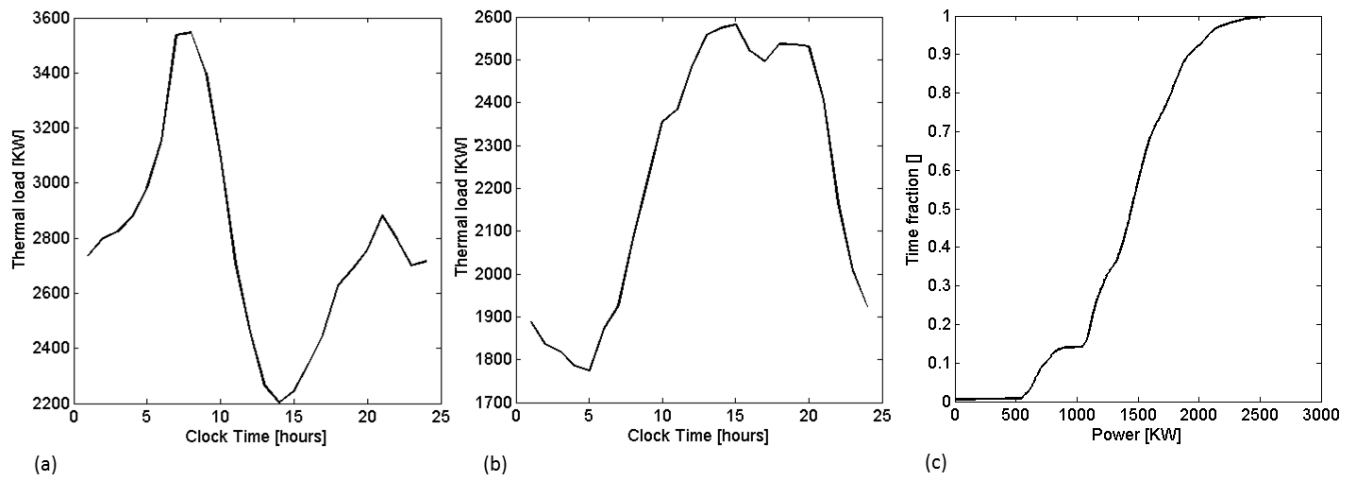
789　**Figure 9. (a): Thermal load on the typical winter day. (b): Thermal load on the typical summer day. (c): Cumulative power**

790　**distribution in the year considered.**

791

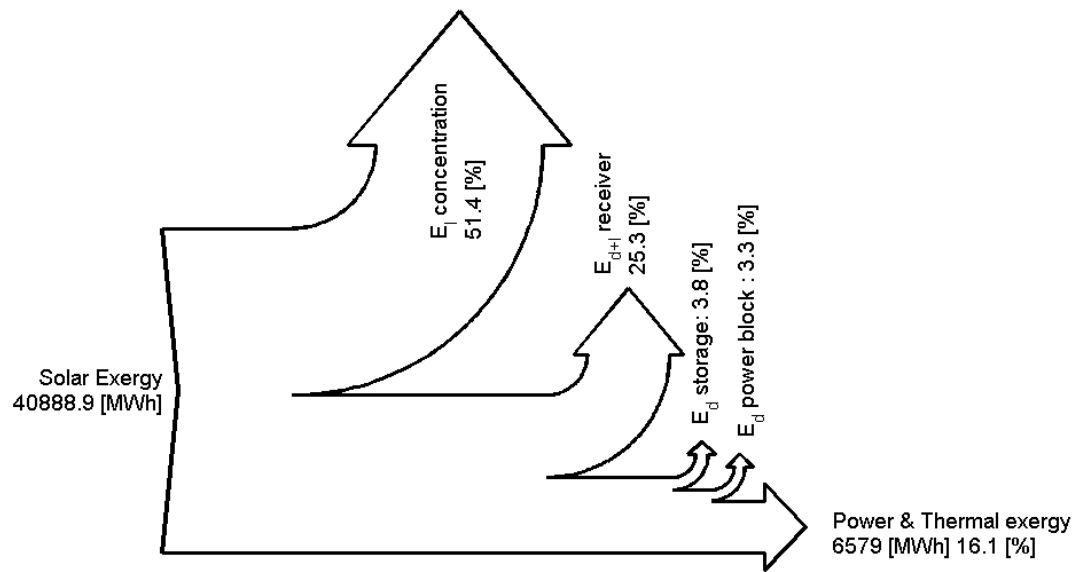**Figure 10. Annual exergy streams of the CSP plant**
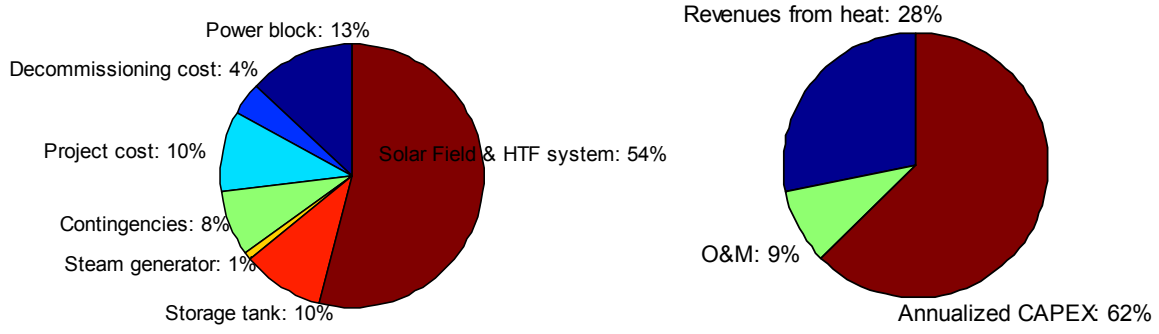
Figure 11. Left: Breakdown of the annualized investment costs, Right: Breakdown of LEC
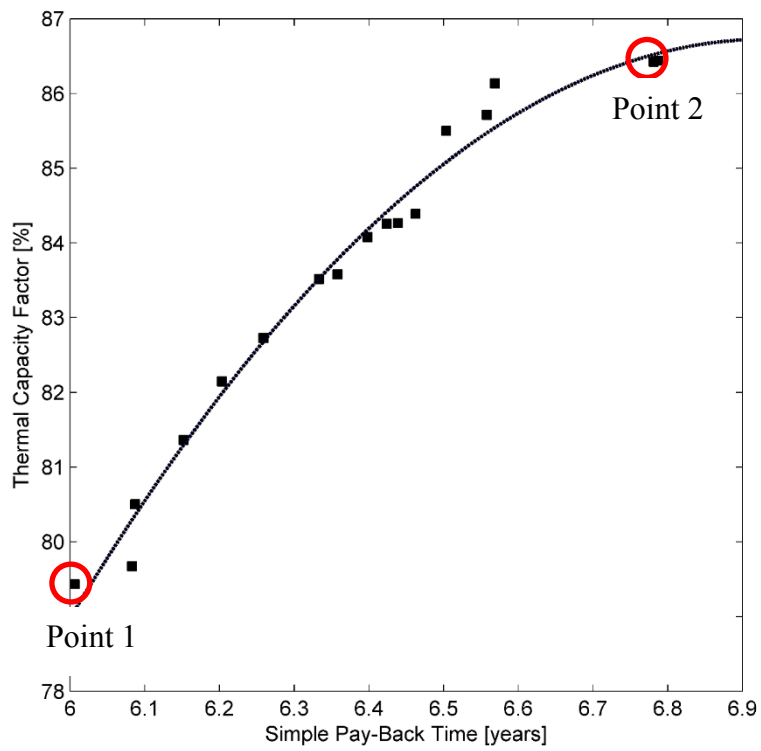
Figure 12. Pareto front: set of solutions of the multi-objective optimizations. Red indicators are obtained by the optimization, the blue solid line is a polynomial regression function used to highlight the trend

798

799
800

801

Point 1

Point 2

Steam Generator: 1%
Decommissioning 4%
Storage tank: 3%
Contingencies 8%
Power block: 20%
Project costs 10%
Water tank 6%
Solar Field and HTF system: 48%

Decommissioning 4%
Steam Generator: < 1%
Storage tank: 5%
Contingencies 8%
Power block: 17%
Project costs 10%
Water tank 11%
Solar Field and HTF system: 45%

802   **Figure**
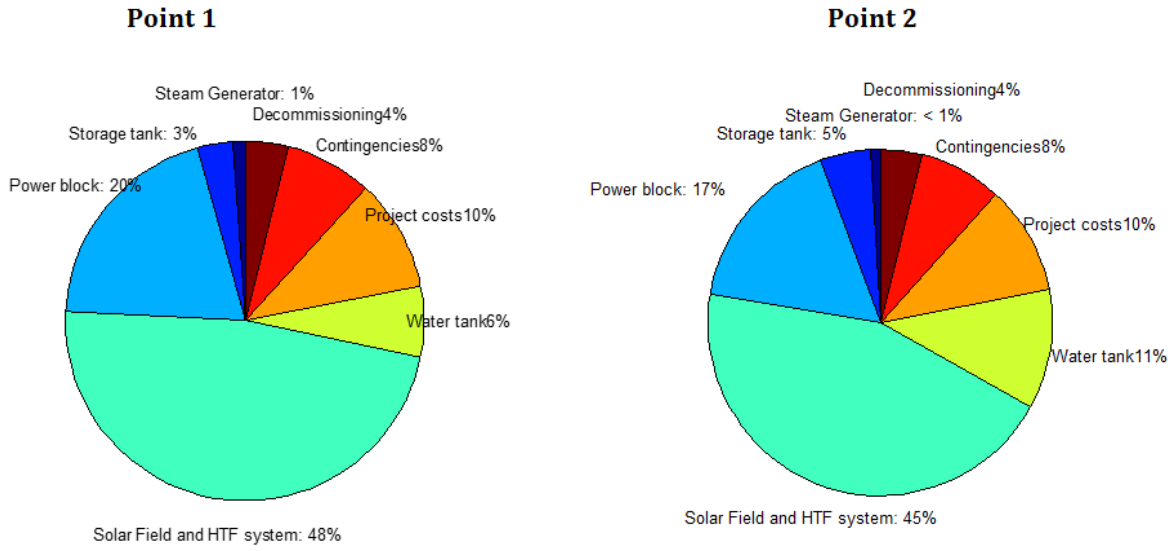
803   **Figure 13 Cost breakdown comparison between the two Pareto points selected**

804

805
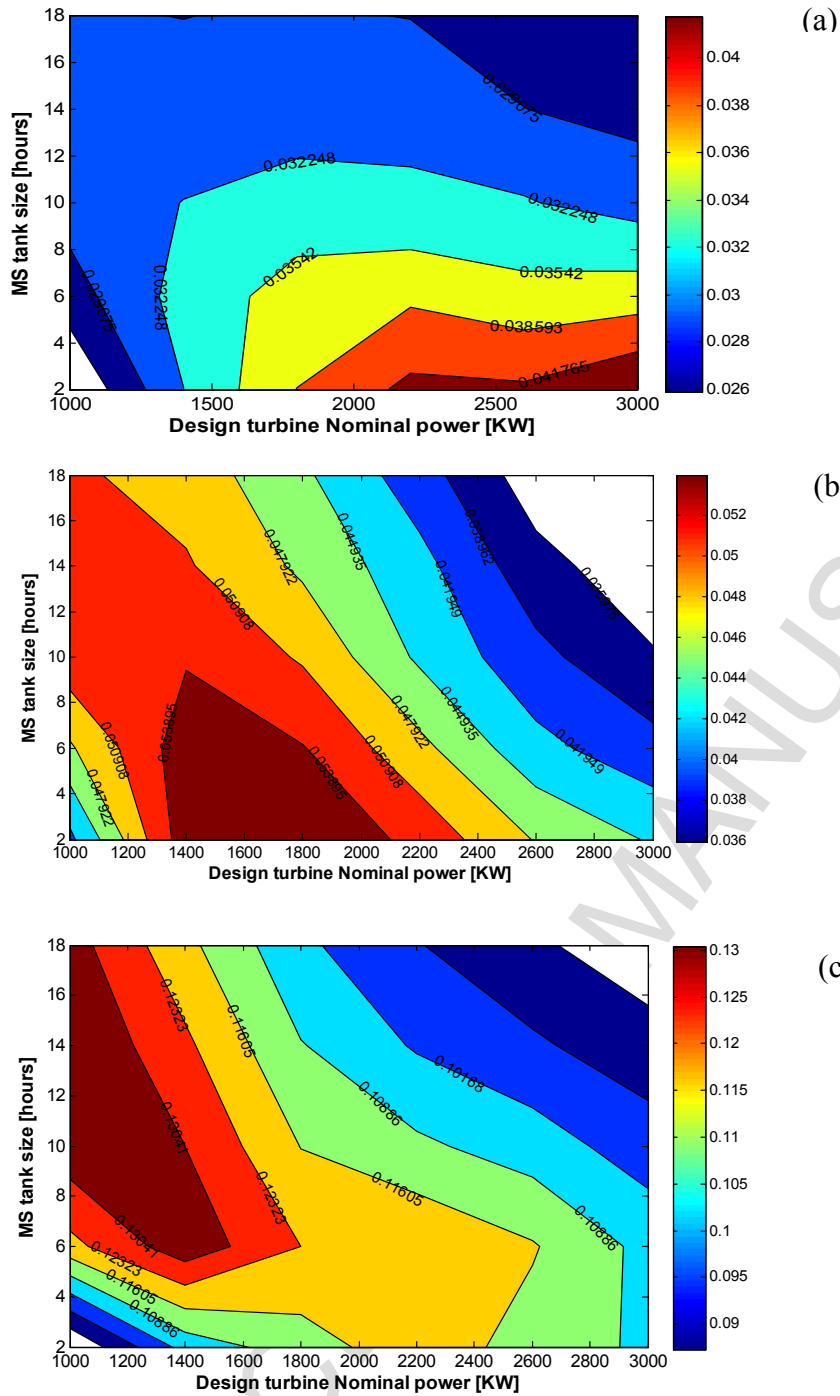
Figure 14. (a):. Revenues from the power market per unit of investment [-]. (b): Revenues from selling heat per unit of investment [-]. (c): Revenues from incentive per unit of investment [-].

806
807

808

Decision variable	Lower bound	Upper bound	Type	Utilizeed in Case 1	Utilized in Case 2
Number of hours of molten storage NH [hours]	1	24	Continuous	Yes	Yes
Tank aspect ratio D/H [-]	0.2	5	Continuous	Yes	Yes
Design Turbine Power P_e [kW]	500	2500	Continuous	No	Yes
Solar Multiple SM [-]	1	8	Continuous	Yes	Yes
Spacing between collectors $d_{spacing}$ [m]	5	25	Continuous	Yes	Yes
Steam generator height H [m]	1	4	Continuous	Yes	Yes
n. of tubes of the steam generator n_{tubes} [-]	3	20	Integers	Yes	Yes
n. of collectors in a string n_{coll}[-]	2	8	Integer	Yes	Yes
Tracking system axis [-]	1 = N-S	2: E-W	Integer	Yes	Yes
Number of hours of water storage NH_{water}[hours]	2	24	Continuous	No	Yes

809   **Table 1. Decision variables overview**

810

DIRECT COSTS	Characteristic dimension	Cost	Unit	n	S_{ref}	Sources
Solar field trough	Mirror surface	357	$/m^2	1	-	[43] & ENEA
Tank Envelope	External surface	2364	$/m^2	0.8	1909	[43]
Fluid, Foundations and Handling system (Tank)	Total volume	1131	$/m^3	0.82	1060	[43] & ENEA
Steam Generator	Number of tubes	11904	$/(n_{tubes})$	0.78	84	ENEA
Steam turbine	Design electric power	473	$/MW	0.67	25	[39]
Condenser	Heat transfer surface	585	$/m^2	1	25	[39]
Pump, BOP, buildings, Safety systems(Power block)	Design electric power	376	$/MW	0.8	110	[39]
Water tank	Total volume	660	$/m^3	1		[47] & ENEA
INDIRECT COSTS						
Engineering, Procurement, Construction & Project costs	-	11.8	% of direct capital cost	-	-	[43]
SERVICES and O&M						
Grounds/house keeping	Ground surface	0.04	$/m^2	-	-	Elaborated from [43]
Mirror washing	Mirror surface	0.41	$/m^2	-	-	[43]
Water Treatment	Design electric power	1318	$/MW	-	-	[43]

Materials Maintenance	-	3.2	% of capital cost	-	-	[43]
TES and Power block Labor	Design electric power	5564	$/(MW y)	-	-	Elaborated from [43]
Solar field Labor	Mirror surface	2.07	$/(m^2 y)	-	-	Elaborated from [43]
OTHER COSTS						
Contingencies	-	10	% of total project cost	-	-	[42]
Decommissioning	-	5	% of total project cost	-	-	[42]
Interest rate	-	7	%	-	-	[39]
Insurance rate	-	2	%	-	-	[39]

811   **Table 2. Summary of economic model data**

812

Hours of storage [-]	14.41
Tank Aspect ratio [-]	1.16
Solar multiple [-]	4.12
Mirror spacing [m]	15.23
Number of collectors per string [-]	8
Height of the steam generator [m]	2.58
Number of tubes of the steam generator [-]	9
Axis tracking	N-S

813 **Table 3. Optimal design in the basic configuration**

814

Total power generation [MWh]	3864
Total heat sold [MWh]	10206
Total heat wasted [MWh]	0
Total auxiliaries [MWh]	117
Capacity Factor [%]	38.64
Power block efficiency [%]	25.41
Optical efficiency solar field [%]	48.55
Thermal efficiency solar field [%]	80.68
System gross electrical efficiency [%]	9.72
System net electrical efficiency [%]	9.45
System total efficiency [%]	38.44

815

Table 4. Energy flows and efficiencies

816

Exergetic Efficiency of concentrating device[%]	48.56
Exergetic Efficiency Receiver [%]	47.87
Exergetic Efficiency Storage [%]	83.48
Exergetic Efficiency Turbine [%]	87.50
Exergetic Efficiency Condenser [%]	84.63
Exergetic efficiency System [%]	16.08

817   **Table 5 Calculated second-law efficiencies of the main components**

818

	Point 1	Point 2
MS storage size [hours]	1.9	3.2
Design Turbine Power [kW]	2294	2366
Solar multiple [-]	1.87	2.1
Height Steam Generator [m]	2.69	2.48
Number of tubes steam generator [-]	12	12
Water storage size [hours]	8.89	18.91
Tracking	E-W	E-W
Direct investment costs [M$]	16.39	19,95
LEC [$/MWh]	296	344
Revenues from heat [k$]	740	794
Revenues from incentive [k$]	2006	2200
Revenues from market [k$]	622	738
Simple Pay-Back Time [years]	6.0	6.8
Capacity Factor power block [%]	24.54	24.94
Thermal Load Capacity Factor [%]	79.22	86.46
Total Power [GWh]	4.71	5.16
Electrical net efficiency [%]	9.32	8.96
Total efficiency [%]	39.62	37.52

819

Table 6. Pareto-point analysis

820